RSC Advances

PAPER

View Article Online
View Journal | View Issue

Cite this: *RSC Adv.*, 2026, **16**, 18612

Hydrogen storage capacity, strain-improved formation enthalpy, desorption temperature, and high energy harvesting performance of $SrGaH_5$

Samia Shahzadi,[a] A. Ibrahim[b] and S. Nazir *[a]

The study of hydrogen storage (HS) characteristics in complex hydrides has become a compelling goal in recent times. Therefore, we explore the $SrGaH_5$ hydride by focusing on its potential for HS utilization and various physical aspects *via* first-principles calculations under hydrostatic strain. The results indicate that strain has a positive impact on the system's thermodynamics, which enhances its potential for practical applications as a HS material. The formation enthalpy and desorption temperature decrease to −42.93/−45.18 kJ per mol H_2 and 306.67/322.74 K under −5%/+5% strain from the unstrained values of −48.03 kJ per mol H_2 and 343.13 K, respectively. These values are nearly ideal, approaching the theoretical values of −40 kJ per mol H_2 and 233–333 K, making it a promising candidate for HS uses. Furthermore, the volumetric hydrogen capacity is enhanced to 17% at −5% and the system exhibits a high gravimetric hydrogen capacity of 3.10%, which is good enough for practical purposes. Along with this, the system is found to be mechanically stable, where the calculated $\frac{G}{B}$ ratio and Poisson's ratio further imply the existence of ionic bonding character in the material. Further, the non-negative phonon frequency curves validate the dynamical stability of the structure. The electronic structure calculations predicted an insulating behavior with an indirect energy gap of 3.58–2.43 eV for the considered strain range. Surprisingly, the thermoelectric performance of the system has been significantly improved under tensile strain as the figure of merit reaches a high value of 0.61 at 550 K under +5% strain. This is because the mean free path of phonons is reduced as the temperature rises due to an increase in phonon scattering driven by greater lattice vibrations, which causes a decrease in lattice thermal conductivity. Hence, the hydrogen storage capabilities and other aspects of the material indicate that it is an appropriate candidate for HS and might be crucial in various energy-generating applications.

Received 15th December 2025
Accepted 9th March 2026

DOI: 10.1039/d5ra09694d

rsc.li/rsc-advances

1 Introduction

Increasing environmental concerns, especially regarding CO_2 emissions from fossil fuels, have driven worldwide investigations into sustainable alternative energy sources to create a more sustainable future. Recent work has been focused on new and renewable sources to meet the growing need for sustainable and affordable energy,[1–3] where fossil fuels persist as the primary source of energy globally. However, the rapid depletion of petroleum resources and the increase in energy demand highlight the importance of sustainable energy sources.[4] They could provide alternative energy sources and be environmentally friendly for countries that lack natural resources. In this sense, hydrogen is a cost-effective and non-toxic energy source that is suitable for mobile and stationary applications[5,6] due to its abundance and reduces reliance on imported oil.[7] However, storing and transporting hydrogen is critical for large-scale applications. Therefore, new hydrogen absorption and storage materials are being developed to ensure long-term safety.[8–10] Compounds that are employed for energy storage must meet certain criteria, including large hydrogen storage (HS) capacities,[11] reversibility,[12] release at ambient conditions,[13] and acceptable kinetics.[14,15] Compared to traditional methods for HS techniques such as gas compression and liquefaction,[16,17] solid-state storage is gaining popularity due to its lightweight, cost-effective, and safer materials.[7,18] In advanced technology, metal and complex metal hydrides,[19,20] intermetallic hydrides,[21–23] complex chemical hydrides,[24] nanostructured carbon materials,[25] and metalorganic compounds have been used extensively.[26–29]

Lately, transition metal (TM)-based perovskite-type hydrides have attracted greater attention from researchers due to their potential uses in HS applications.[30] Gencer *et al.*[7] determined a hydrogen $T_{des.}$ (desorption temperature) of 446.3 K, 419.5 K, and 367.5 K for $LiNiH_3$, $NaNiH_3$, and $KNiH_3$ systems,

[a]*Department of Physics, University of Sargodha, 40100 Sargodha, Pakistan. E-mail: safdar.nazir@uos.edu.pk; Tel: +92-334-9719060*

[b]*Department of Physics, College of Science, King Khalid University, P. O. Box: 9004, Abha, Asir, Postal Code: 61413, Kingdom of Saudi Arabia*

respectively. Furthermore, Xiong *et al.*[31] reported that $NaRuH_3$ and $NaRhH_3$ have high gravimetric HS capacities ($C_{wt\%}$) of 2.38 wt% and 2.35 wt%, respectively. However, their potassium analogs ($KRuH_3$/$KRhH_3$) have somewhat lower values (2.11/2.09 wt%). Interestingly, the $T_{des.}$ drops from 436.40 K ($NaRuH_3$) to 286.37 K ($KRhH_3$), indicating enhanced reversibility in potassium-based systems. Along with this, ARH_3 shows potential for H_2 storage applications due to its impressive $C_{wt\%}$ of 6.042 wt% for $LiCaH_3$ and 3.678 wt% for $KCaH_3$. Moreover, these materials satisfied the criteria for Born stability based on their mechanical parameters, which are derived from elastic constants, including Pugh's ratio $\left(\frac{B}{G}\right)$ and the related moduli. The analysis of the $\frac{B}{G}$ ratio and Cauchy pressure (C_P), indicates that, unlike other compounds, $KCaH_3$ exhibits a ductile nature (Poisson's ratio (ν) = 0.29).[32] Besides this, alkali metals containing ternary hydrides, such as $LiBH_4$ (LBH), $LiAlH_4$, $NaBH_4$, and $NaAlH_4$, have been intensively explored as prospective HS materials (HSMs) due to their high $C_{wt\%}$.[33–36] Among them, LBH is found to be a promising solid-state HSM with a volumetric capacity ($\rho_{vol.}$) of 121 kg H_2 per m^3 and the highest $C_{wt\%}$ of 18.3 wt% at room temperature.[35,37,38] In 1997, $NaAlH_4$ was introduced as a lightweight reversible HSM and is regarded as a promising material for solid-state hydrogen storage due to its high $C_{wt\%}$, widespread availability, and low cost.[33] According to Vajeeston *et al.*,[39] the alkali boron tetrahydrides ABH_4 (where A = Li, Na, K, Rb, and Cs) are insulators having an energy gap (E_g) ranging from 5.5 to 7.0 eV. Recent experimental evidence indicates that $LiAlH_4$ and $NaAlH_4$, processed by mechanochemical means under ambient conditions with specific TM catalysts,[40] can rapidly release 7.9 and 5.6 wt% of hydrogen, respectively. The theoretical $C_{wt\%}$ of $LiAlH_4$ is as high as 10.6 wt%.[41] In contrast to other chemical hydrides, which are simple and stable,[42] $NaBH_4$ is regarded as a potential candidate for HSMs due to its high hydrogen concentration of 10.6 wt%.

To improve the stability (formation enthalpy (ΔH_f)/$T_{des.}$) of the HSMs, numerous theoretical and experimental studies have been conducted, where size reduction,[28,43] alloying,[44,45] doping/functionalization,[46,47] morphological control,[48,49] and strain engineering[50,51] are some of the most promising approaches that accomplish that goal. The calculations conducted by Zhang *et al.*[52] indicated that under biaxial compressive and tensile strains, the $\Delta H_f/T_{des.}$ and hydrogen diffusion observed for magnesium hydride (MgH_2) decreased simultaneously, thereby enhancing its potential for HS applications. Similarly, LBH maintains its high $C_{wt\%}$ (18.3 wt%), while biaxial strain improves the thermodynamic characteristics as well as hydrogenation kinetics,[50] to make it a superior candidate for energy transport in mobile applications. Specifically, under compression of −6%, the ΔH_f changes from −71.30 kJ per mol H_2 in unstrained $MgCoH_3$ to −37.29 kJ per mol H_2, and the $T_{des.}$ decreases to 285.34 K as opposed to 545.52 K, which are both near ideal values (−40 kJ per mol H_2 and 289–393 K) for practical applications.[53] Likewise, the ΔH_f and $T_{des.}$ are observed to decrease from −67.73 kJ per mol H_2 and 521 K for unstrained $ZrNiH_3$ to −33.73 kJ per mol H_2 and 259.5 K under a maximal biaxial compressive strain of −6%, correspondingly.[54] Additionally, for a maximal biaxial tensile strain of +6%, the values are −50.99 kJ per mol H_2 and 392.23 K. A similar phenomenon has also been noted for uniaxial strain, wherein the $\Delta H_f/T_{des.}$ are reduced to −39.36 kJ per mol H_2/302.78 K for a maximum uniaxial compressive strain of −12% and to −51.86 kJ per mol H_2/399 K under a maximum uniaxial tensile strain of +12%.[54]

The aforementioned considerations clearly illustrate that strain engineering serves as an effective strategy for optimizing the HS features and overall physical attributes of materials. Various ABH_5-type hydrides like $CaAlH_5$ (a novel member of the aluminum hydride family, where $Ca(AlH_4)_2$ breaks down to generate $CaAlH_5$),[55] $BAlH_5$ (B = Ba, Mg)[56] (where the experimentally determined crystal structure of $BaAlH_5$ is confirmed, while the $MgAlH_5$ structure is computationally predicted), $MgGaH_5$, $CaGaH_5$, $BaGaH_5$, and $SrGaH_5$ (SGH)[57] have been extensively studied *via* both theoretical and experimental investigations. Nevertheless, no prior research has looked at the ability to store hydrogen, despite extensive structural analyses of SGH. Therefore, we theoretically examine the effects of hydrostatic strain on the structural, HS, mechanical, dynamical, electronic, and thermoelectric (TE) performance of SGH in the context of HS applications. A detailed investigation is performed to assess its structural stabilities and HS aspects, including ΔH_f, $T_{des.}$, $C_{wt\%}$, and $\rho_{vol.}$. The findings offer important insights into the strain-dependent behavior of SGH, serving as a guide for its practical application in HS technologies. Moreover, under tensile strain, the TE performance is much improved and a particularly high *ZT* is achieved at high temperature.

2 Computational detail

The full-potential linearized augmented plane-wave approach as implemented in the WIEN2K code[58] was used to perform density-functional-theory-based computations for the current study. The exchange–correlation functional, which is parameterized in terms of a generalized gradient approximation (GGA), is utilized.[59] The plane-wave cutoff is set at $R_{mt} \times K_{max} = 5$ with $G_{max} = 20$ for the wave-function expansion inside the atomic spheres, and a maximum value of $\ell_{max} = 12$ is selected. It is found that a 7 × 7 × 9 *k*-space grid with 128 points inside the irreducible Brillouin zone wedge gives effective convergence. Additionally, in every case, the complete relaxation of the atomic positions by reducing the atomic forces up to 2 mRy per a.u. is considered. It is expected that self-consistency occurs when the total energy (E_t) convergence is smaller than 10^{-5} Ry.

3 Results and discussion

3.1 Crystal structure

The SGH crystal has an orthorhombic structure with space group $Pna2_1$ (no. 33) and its primitive unit cell is composed of 28 atoms with 4/4/20 ions of Sr/Ga/H, having lattice constants a = 8.63559, b = 8.79764, and c = 4.71862.[57] The Wyckoff positions of the Sr, Ga, H_1, H_2, H_3, H_4, and H_5 are 4a (0.9935493, 0.8164696, 0.9540590), 4a (0.8332764, 0.4158104, 0.9539526), 4a

(0.2739413, 0.1710615, 0.2299465), 4a (0.0183018, 0.4022104, 0.9541427), 4a (0.9811656, 0.0881250, 0.9541069), 4a (0.2259233, 0.6709108, 0.1778099), and 4a (0.7819938, 0.5906299, 0.9539823), respectively.[57] The schematic representation of the crystal structure of SGH in various orientations is shown in Fig. 1. In any material computation science, optimizing the structural parameters is a crucial phase that yields important details about the material under study. The goal is to identify the optimum values for the structural parameters that are required for an accurate description, where the optimized unit cell volume and associated ground-state energy (E_0) have been determined. Using the ground-state volume optimization curve, Birch Murnaghan's equation of states[60] was applied to get optimized lattice constants, the compressibility modulus (B), and its first derivative (B') for the SGH hydrides as follows:

$$E(V) = E_0 + \frac{BV}{B'\left(B'-1\right)}\left(B\left(1-\frac{V_0}{V}\right)+\left(\frac{V_0}{V}\right)^{B'}-1\right) \quad (1)$$

Fig. 2 illustrates the variance of E_t as a function of volume and presents the results of the optimization process. The curve generally displays a minimum, indicative of the equilibrium volume at which the system attains the E_0 configuration. The optimized lattice parameters of SGH are $a = 8.63567$, $b = 8.79852$, and $c = 4.71772$ Å at the lowest volume, as mentioned in Table 1 along with the calculated $B/B'/E_0$.

3.2 Thermodynamic stability and desorption temperature

Next, we computed ΔH_f, which serves as a crucial thermodynamic parameter for the identification and classification of HSMs. It enables the assessment of the heat generated by the overall hydration reaction, which subsequently facilitates the determination of the $T_{des.}$. The following expression is used to evaluate the ΔH_f:[61]

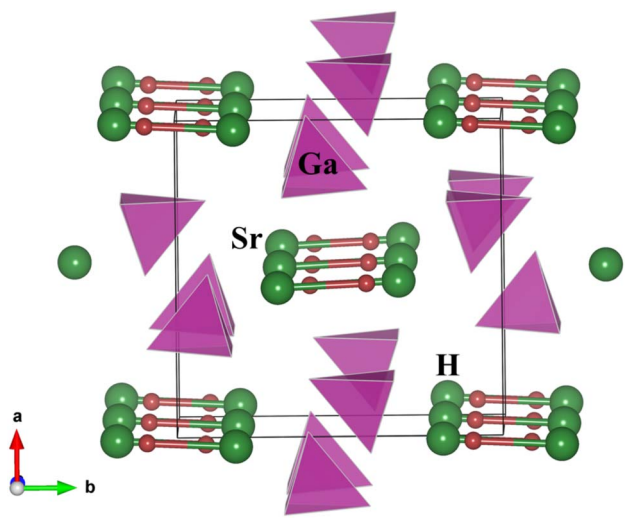

Fig. 1 Orthorhombic structure of $SrGaH_5$ hydride (purple: GaH_4 tetrahedron).

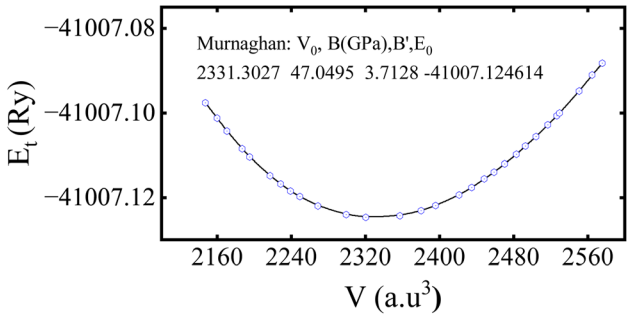

Fig. 2 Computed total energy (E_t) as a function of volume (V_0) of the $SrGaH_5$ hydride.

$$\Delta H_f = \frac{1}{N_{Sr}+N_{Ga}+N_H}\left[E_t^{SrGaH_5}-\left(N_{Sr}E_{bulk}^{Sr}+N_{Ga}E_{bulk}^{Ga}+N_HE_{bulk}^{H}\right)\right] \quad (2)$$

$E_{bulk}^{SrGaH_5}/E_{bulk}^{Sr}/E_{bulk}^{Ga}/E_{bulk}^{H}$ and $N_{Sr}/N_{Ga}/N_H$ represent the E_t of the SGH/Sr/Ga/H in their bulk stable phases and total number of atoms of Sr/Ga/H in each case, respectively. Moreover, the hydrogen reference state used in this work is isolated H_2. All energies were obtained from fully relaxed structures under each strain condition. Also, the formation enthalpy is reported in units of kJ per mol H_2, which is the standard convention adopted in previous theoretical and experimental hydrogen storage studies. Using the same reference state and units allows direct comparison with previously reported hydrides in the literature.[62–64] Thus, compared to the ideal value of −40 kJ per mol H_2,[65,66] our calculated ΔH_f of the unstrained SGH system is −48.03 kJ per mol H_2, which is a bit higher and may reduce the system's functionality for the HS application. This is because, due to the substantial energy required for hydrogen absorption or desorption, a system with a reasonable ΔH_f is considered the most stable.[67] Here, we would like to emphasizes that the present calculations did not include contributions due to zero-point energy (ZPE) and finite-temperature contributions associated with vibrations. All of the ΔH_f are reported to be the total energies of the ground states of the DFT calculations at 0 K with no phonon corrections. The ZPE may have a significant role to play in hydride systems because of the low mass of hydrogen atoms, and ZPE and vibrational terms can alter the absolute values of the ΔH_f at least modestly and, as a result, the $T_{des.}$ calculated can be inaccurate. But, as our work is based on comparative trends due to applied strain, the relative stability and strain-dependent behavior should not be qualitatively affected. Along with this, the hydrogen $T_{des.}$ is also a critical factor to consider when choosing a HS system, which must be maintained between 233 and 333 K as stated by Kudiiarov *et al.*[68] Hence, the accurate determination of $T_{des.}$ is crucial for assessing the efficiency and appropriateness of a HSM for many applications. It can be determined utilizing the conventional Gibbs equation, as illustrated in the subsequent formula:

$$\Delta G = \Delta H_f - T\Delta S \quad (3)$$

Table 1 Computed lattice constants (*a*, *b*, *c*) in Å, volume (*V*) in a.u^3, bulk modulus (*B*) in GPa, *B*′, and ground-state energy (E_0) in Ry for the $SrGaH_5$ hydride

$SrGaH_5$	*a*	*b*	*c*	*V*	*B*	*B*′	E_0
	8.63567	8.79852	4.71772	2331.30	47.05	3.7128	−41 007.124614

Under normal conditions of pressure and temperature, $\Delta G = 0$, enabling us to get $T_{\text{des.}}$ as follows:

$$T_{\text{des.}} = \frac{\Delta H_f}{\Delta S} \quad (4)$$

here ΔS represents the change in entropy and its estimated value of ΔS falls within the range of 95–140 J per mol H_2 (Zhou *et al.*[69]). For the present work, $\Delta S = 140$ J per mol H_2 is used. Hence, the corresponding $T_{\text{des.}}$ of SGH is 343.13 K, which does not fall within the required range (233–333 K).[68] Consequently, the objective of this investigation is to enhance the HS features of the material by diminishing its stability. To achieve this objective, we adjusted the hydrostatic strain, ranging from −5% to +5% along the *abc*-axes, to enhance the de-hydrogenation features (ΔH_f and $T_{\text{des.}}$) of the material. The hydrostatic strain (ε) is defined as:

$$\varepsilon(\%) = \frac{a/b/c - a_0/b_0/c_0}{a_0/b_0/c_0} \times 100\% \quad (5)$$

where $a/b/c$ and $a_0/b_0/c_0$ denote the lattice constants along the *x*/*y*/*z*-axis of the SGH unit cell with and without deformation, respectively. Fig. 3(a) depicts the response of the cell parameters of the SGH system under strain. For an applied compressive strain of −5%, $a/b/c$ reduces until it attains a minimum value of 8.20381/8.35776/4.48269 Å. This signifies a decrease in the unit cell volume, as presented in Fig. 3(b)(left). Conversely, when subjected to tensile strain, $a/b/c$ grows until it attains its maximum value of 9.06737/9.23752/4.95455 Å at +5%, which is accompanied by an augmentation of the cell volume. Fig. 3(b)(right) will be discussed later. Now, we analyze the effects of strain on ΔH_f and $T_{\text{des.}}$. It is noteworthy that by applying strain, $\Delta H_f/T_{\text{des.}}$ decreases and we achieve the desired range at a maximum considered strain range of ±5%, as shown in Fig. 4(a)/(b). As Fig. 4(a) illustrates, the ΔH_f exhibits a decrease from −48.03 to −42.93 and −45.18 kJ per mol H_2 for −5% compressive and +5% tensile deformations, respectively. The values presented here are considerably closer to the optimal ΔH_f of −40 kJ per mol H_2 when contrasted with the unstrained structure. These findings are consistent with those presented by Rkhis *et al.*,[54] where the authors found that the thermodynamic stability of the $ZrNiH_3$ perovskite type is diminished under uniaxial/biaxial tensile and compressive stress. Likewise, Benzidi *et al.*,[50] demonstrated that deformation significantly influences the thermodynamic properties of LBH as well. They observed the application of biaxial compressive and tensile deformation results in a reduction of the material's stability, which means hydrogen reversibility is enhanced under strain. Under −5% compressive strain, the system exhibits maximum hydrogen reversibility. Further to this, the strain-tuned $T_{\text{des.}}$ values are displayed in Fig. 4(b), which shows a decrease from 343.13 K to 306.67/322.74 K for compressive/tensile deformation of −5%/+5%. Further, compression-induced deformation diminishes the unit-cell volume and the interatomic distances, resulting in enhanced atomic interactions and reducing the material stability. On the other hand, tensile deformation enhances the volume of the unit cell and the interatomic distance, resulting in atomic dispersion and a reduction in both the ΔH_f and $T_{\text{des.}}$. Therefore, the stability of a material appears to be correlated with its volume, as suggested by Willems *et al.*,[70] who reported a link between stability and $\frac{\Delta V}{V}\%$. Similarly, the ΔH_f (see Fig. 5(a)) and $T_{\text{des.}}$ (see Fig. 5(b)) diminish as the $\frac{\Delta V}{V}\%$

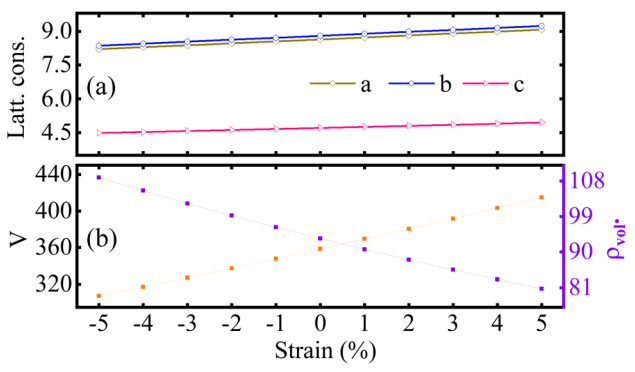

Fig. 3 Calculated (a) optimized lattice constants (Latt. cons.) in Å, (b-left) unit-cell volume (*V*) in Å^3, and (b-right) volumetric capacity ($\rho_{vol.}$) in g H_2 per L as a function of ±5% hydrostatic strain for the $SrGaH_5$ hydride.

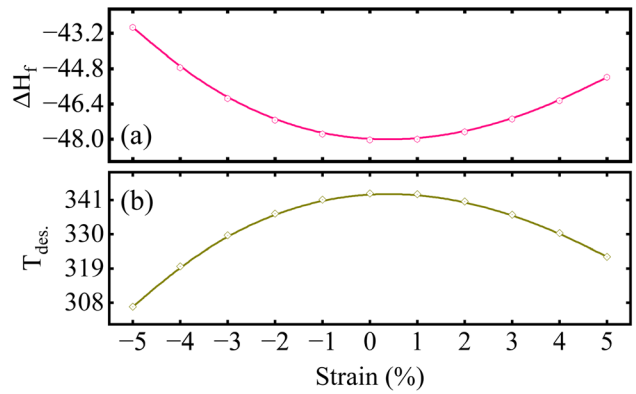

Fig. 4 Computed (a) formation enthalpy (ΔH_f) in KJ per mol H_2 and (b) desorption temperature ($T_{\text{des.}}$) in K for the $SrGaH_5$ hydride as a function of ±5% hydrostatic strain.

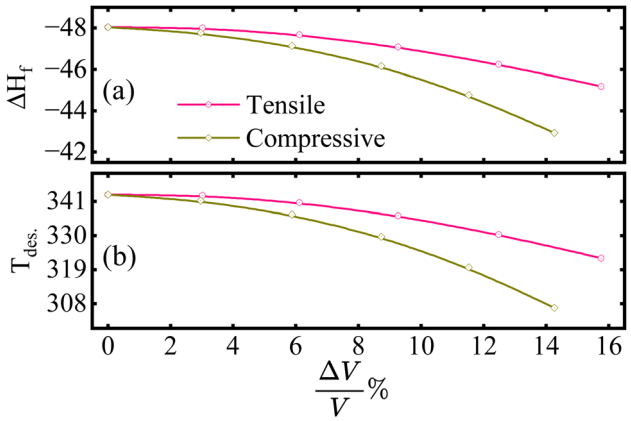

Fig. 5 Computed (a) formation enthalpy (ΔH_f) in KJ per mol H_2 and (b) desorption temperature ($T_{des.}$) in K for the $SrGaH_5$ hydride as a function of $\frac{\Delta V}{V}$%.

increases in the present case as well. Hence, a large $\frac{\Delta V}{V}$% indicates a high material instability.

The estimated ΔH_f and $T_{des.}$ of SGH validate its thermodynamic stability at 0 K and moderate temperature hydrogen release. To investigate the structural changes that occur during desorption, we consider the subsequent thermal decomposition of the system proceeds *via* the breakdown of Ga–H and Sr–H bonds, resulting in the release of hydrogen gas and the creation of SrH_2 along with metallic Ga. While subjected to heat, it undergoes thermal decomposition, as described by the reaction: $SrGaH_5 \rightleftharpoons SrH_2 + Ga + \frac{3}{2}H_2$. Along with this, the reverse process, specifically rehydrogenation, takes place under appropriate hydrogen pressure and reduced temperatures as follows: $SrH_2 + Ga + H_2 \rightleftharpoons SrGaH_5$. This reformation is thermodynamically viable and illustrates the reversible characteristics of SGH, highlighting its promise for practical HS applications. Now, the influence of bonding on enhancing HS features under hydrostatic strain of −5%/0%/+5% can be elucidated through the analysis of electron density distributions (EDDs; see Fig. 6(a)/(b)/(c)). Distinct responses are noted for ionic Sr–H and covalent Ga–H bonds. Table 2 illustrates that Ga–H bond lengths exhibit a consistent increase from −5% to +5% strain, leading to a decrease in covalent character (see Fig. 6) and a slight enhancement in H_2 mobility. In contrast, Sr–H bonds exhibit asymmetric elongation, where −5% compressive strain leads to greater expansion compared to +5% tensile strain. This phenomenon directly destabilizes the ionic framework by lowering ΔH_f (see Fig. 4) and significantly enhances the reversibility of hydrogen. This specific behavior elucidates why a −5% strain optimally enhances HS performance; the reason is that the diminished Sr–H interactions reduce the energy barrier for H_2 release, while the maintained Ga–H covalent network facilitates efficient rehydrogenation. Thus, the enhanced reversibility arises from this dual mechanism; weakened ionic bonds promote desorption, whereas preserved covalent bonds ensure cyclability.

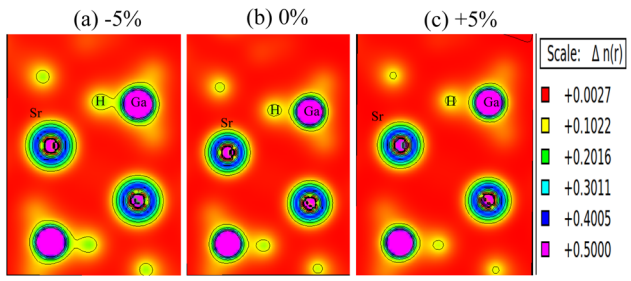

Fig. 6 Computed electron density distribution of the $SrGaH_5$ hydride under (a)−5%, (b) 0%, and (c) +5% hydrostatic strain.

Now, the $\rho_{vol.}$ and $C_{wt\%}$ (ref. 71) of SGH are calculated to predict their future use in HS as follows:[72]

$$\rho_{vol.} = \frac{N_H M_H}{V N_A} \quad (6)$$

$$C_{wt\%} = \frac{\left(\frac{H}{M}\right) M_H}{\left(\frac{H}{M}\right) M_H + M_{Host}} \times 100 \quad (7)$$

The amount of hydrogen that can be stored in a given volume is indicated by $\rho_{vol.}$ (see eqn (6)), where $N_H/M_H/N_A$ represents the number of hydrogen atoms/mass of hydrogen/Avogadro's number. Hence, the computed $\rho_{vol.}$ of the unstrained system is 93.36787 g H_2 per L, which increases to 108.89969 g H_2 per L under −5% compressive strain and decreases to 80.65468 g H_2 per L for +5% tensile strain. The linear trend of $\rho_{vol.}$ against strain is illustrated in Fig. 3(b)(right), which offers significant insights that the HS capacity of the SGH responds to strain, along with the relationship between modifications in the material's structure and the potential for HS. The findings indicate that careful control of the strain conditions throughout the HS process is crucial for attaining maximum HS capacity. For practical hydrogen storage systems, the U.S. Department of Energy (DOE) has established system-level targets of approximately 40 g H_2 per L for $\rho_{vol.}$. These standards have been commonly used to measure the performance of materials. Moreover, the $C_{wt\%}$ refers to the quantity of hydrogen stored per unit mass of a substance and is calculated in eqn (7), where $\frac{H}{M}$ denotes the ratio of hydrogen to material atoms, M_H represents the molar mass of hydrogen, and M_{Host} signifies the molar mass of the host material. The determined value of $C_{wt\%}$ is 3.10%, which means that the material exhibits a commendable hydrogen storage capacity, making it a suitable candidate for HS applications. Along with this, compared to associated high-energy complex hydrides, $BeAlH_5$ has an extremely high gravimetric capacity of 12.19 wt%, which is well beyond the DOE's ultimate target. $CaAlH_5$ attains 6.9 wt%, whereas $SrAlH_5$ attains 4.17 wt%, which is well under the practical standard. Likewise, $BeAlH_5$ has a $\rho_{vol.}$ of 74 g H_2 L, which is much higher than the DOE 2025 objective of 40 g H_2 per L.[73] Thus, compared to these systems, $SrGaH_5$ has a $C_{wt\%}$ of 3.10% and $\rho_{vol.}$ of 93.36787 g H_2

Table 2 Computed nine independent elastic constants (C_{ij}) and the interatomic distances between Sr/Ga and H (Sr–H/Ga–H) in Å for the $SrGaH_5$ hydride under −5%/0%/+5% hydrostatic strain

Strain	C_{11}	C_{12}	C_{13}	C_{22}	C_{23}	C_{33}	C_{44}	C_{55}	C_{66}	Sr–H	Ga–H
−5%	76.19	28.52	27.00	76.33	29.74	103.06	21.12	28.489	24.09	2.69	1.51
0%	47.25	13.07	11.48	50.09	11.14	67.56	14.85	22.96	18.99	2.55	1.59
+5%	35.24	10.13	11.24	34.23	10.02	51.48	9.24	14.10	10.94	2.68	1.67

per L. It has a lower capacity than $BeAlH_5$ but is comparable to $CaAlH_5$.

3.3 Mechanical stability

The elastic constant quantifies the stiffness of a material against applied strain and is essential for evaluating the material's mechanical behavior. In this context, nine independent elastic constants (C_{ij}) for the orthorhombic structure of SGH are computed, utilizing conventional strain and stress relationships[74,75] according to the fundamental Born criteria, expressed as: $C_{11} > 0$, $C_{11}C_{22} > C_{12}^2$, $C_{11}C_{22}C_{33} + 2C_{12}C_{13}C_{23} - C_{11}C_{23}^2 - C_{22}C_{13}^2 > 0$, and $C_{44} > 0$; $C_{55} > 0$; $C_{66} > 0$.[76] The computed values of C_{ij} (see Table 2) can be utilized in determining several physical parameters, including the Bulk modulus (B), Shear modulus (G), and Young's modulus (Y). B quantifies the resistance to volumetric change under applied pressure. The highest value of B is obtained at −5%, denoting the maximum resistance to compression. Also, it has the maximum G/Y of 25.75/65.31, enabling it to endure more transverse deformation as compared to 0% and +5% (see Fig. 7).

Furthermore, the brittleness or ductility of a material may be ascertained using the $\frac{B}{G}$ ratio. A brittle material possesses a $\frac{B}{G}$ below 1.75, whereas a ductile one has a ratio over the threshold of 1.75.[77] The analyzed material under 0% and +5% strain exhibits brittleness, possessing a $\frac{B}{G}$ below 1.75, and is ductile under −5%, as displayed in Fig. 8(a). Similarly, the $\frac{G}{B}$ ratio (also known as Pugh's modulus), as presented in Fig. 8(b), can be utilized to ascertain the bonding aspects of a material. If the $\frac{G}{B}$ is around 0.6, ionic bonding prevails and conversely with a ratio of 1.1, covalent bonding is dominant.[78] Now, ν can be utilized to ascertain the bonding features of a material. It quantifies the expansion or compression in the perpendicular axes relative to the direction of compression or stretching. If its value is 0.1, the material exhibits dominantly covalent bonding, whereas at around 0.25, it demonstrates principally ionic bonding.[79] From Fig. 8(b), the analyzed compound for the strain range −5% to +5% has a ν of around 0.25, indicating a dominance of ionic bonding. Hence, for the examined material under 0% and +5% strain, the dominance of the ionic bonding is confirmed by the $\frac{G}{B}$ ratio and ν.

Along with this, utilizing the ELATE tool,[80,81] we have calculated the elastic anisotropy features of the material subjected to strain. Fig. 9 depicts the fluctuation of anisotropic elastic aspects, specifically Y, linear compressibility (β), G, and ν, subject to various applied strain values. It is found that Y demonstrates directional dependence (see Fig. 9(a)), exhibiting a significant anisotropy under compressive strain and displays a more uniform distribution under strain, signifying strain-induced stiffening or softening in certain crystallographic orientations. Fig. 9(b) shows the directional β, which exhibits an increasing amplitude and anisotropy with the application of tensile strain, indicating that the material becomes more compressible along certain axes under tension. The G in Fig. 9(c) displays considerable anisotropy across the strain range with marked variations in magnitude and distribution, reflecting the impact of strain on the material resistance to deformation. Further, ν in Fig. 9(d) indicates that directional

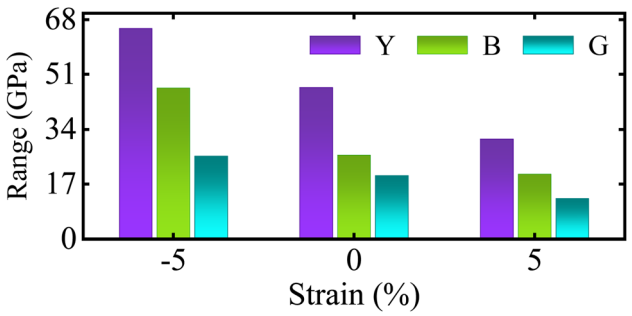

Fig. 7 Computed Young's modulus (Y), Bulk modulus (B), and Shear modulus (G) of the $SrGaH_5$ hydride under −5%/0%/+5% hydrostatic strain.

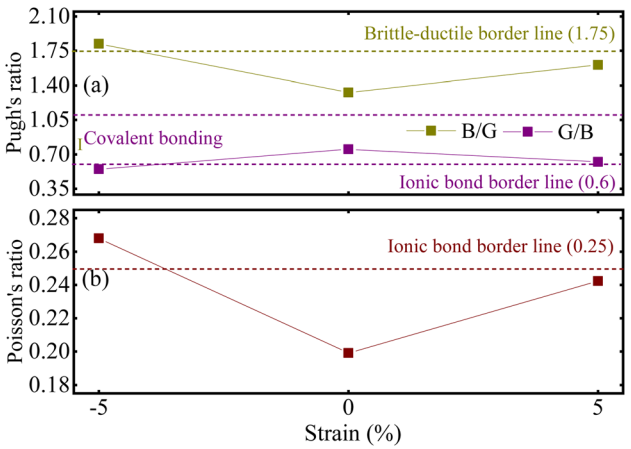

Fig. 8 Computed (a) Pugh's ratio $\left(\frac{B}{G}/\frac{G}{B}\right)$ and (b) Poisson's ratio (ν) of the $SrGaH_5$ hydride under −5%/0%/+5% hydrostatic strain.

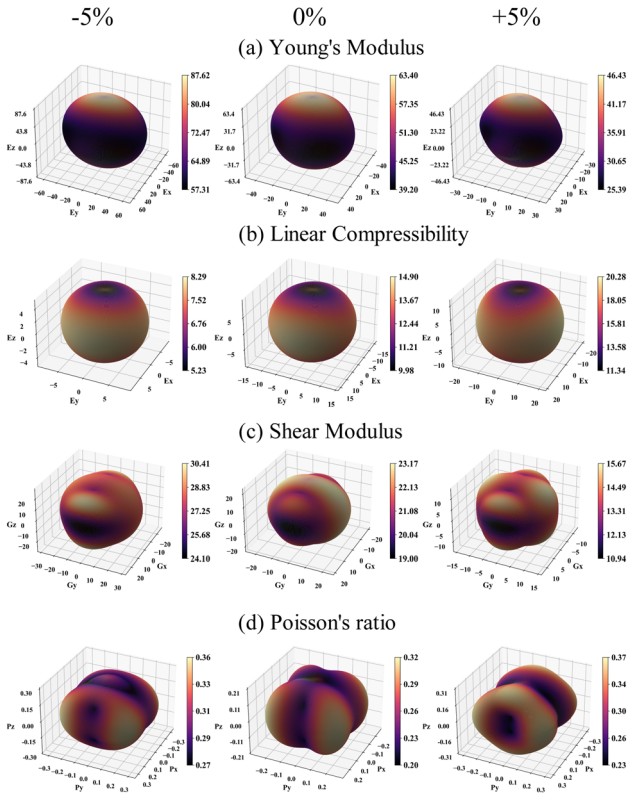

Fig. 9 Directionally dependent (a) Young's modulus (Y), (b) linear compressibility (β), (c) Shear modulus (G), and (d) Poisson's ratio (ν) for the $SrGaH_5$ hydride under −5% (left column)/0% (middle column)/+5% (right column) hydrostatic strain.

variations reflect strain-induced alterations in lateral deformation behavior. Hence, Fig. 9 highlights that strain engineering not only adjusts the elastic constants but also enhances the anisotropic mechanical response of the materials (Table 3).

3.4 Dynamical stability

Next, to verify the dynamical stability of the system, phonon computations were conducted. Fig. 10(a)/(b)/(c) shows a graph of the computed phonon spectrum under −5%/0%/+5% hydrostatic strain. The number of phonon branches in a unit cell is exactly proportional to three times the number of atoms, with each atom normally contributing three phonon branches. It exhibits 3 acoustic and $3n - 3$ optical modes that make up the

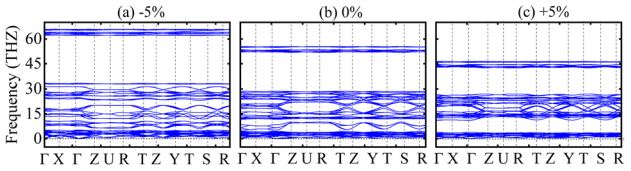

Fig. 10 Computed phonon dispersion curves of the $SrGaH_5$ hydride under (a) −5%, (b) 0% and (c) +5% hydrostatic strain.

$3n$ total branches.[82] The SGH structure includes 84 vibrational modes, including 3 acoustic and 81 optical modes, and its fundamental unit cell has 28 atoms. The three calculated phonon dispersion curves for the −5%/0%/+5% strain (see Fig. 10) do not contain any negative frequencies, which confirms that they are dynamically stable as well. Furthermore, Fig. 11 displays the computed phonon lifetime of the unstrained motif, which shows a high correlation between the phonon spectra (see Fig. 10(b)) and the phonon lifetime. The linear dispersion of the acoustic modes around Γ, which has limited scattering phase-space and large group velocities, is the source of the long lifetime of low-frequency phonons (<0.3 THz). The flat optical branches, on the other hand, have low group velocities and high density of states, which encourage rapid anharmonic decay, and are consistent with the short lifetime of high-frequency phonons (>0.3 THz).

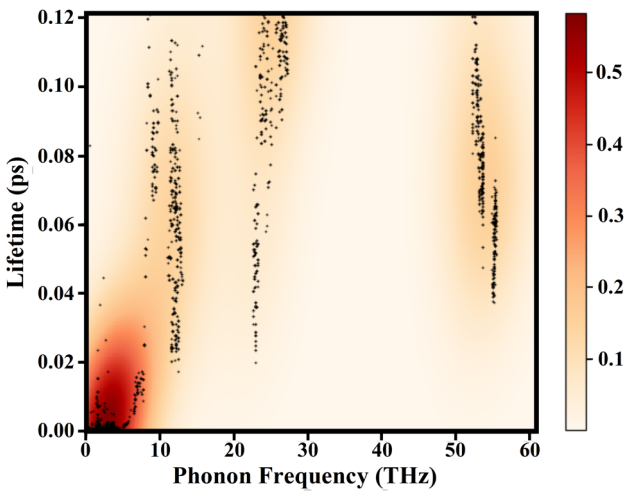

Fig. 11 Computed phonon lifetime of the unstrained $SrGaH_5$ hydride.

Table 3 Computed minimum/maximum values of Young's modulus (Y_{min}/Y_{max}) in GPa, linear compressibility (β_{min}/β_{max}) in TPa^{-1}, Shear modulus (G_{min}/G_{max}) in GPa, Poisson's ratio (ν_{min}/ν_{max}), and their corresponding anisotropic factors (A) for the $SrGaH_5$ hydride under −5%/0%/+5% hydrostatic strain

	Young's modulus			Linear compressibility			Shear modulus			Poisson's ratio		
Strain	Y_{min}	Y_{max}	A	β_{min}	β_{max}	A	G_{min}	G_{max}	A	ν_{min}	ν_{max}	A
−5%	57.14	87.62	1.53	5.23	8.28	1.58	21.12	30.41	1.44	0.17	0.39	2.27
0	39.51	63.40	1.60	9.98	14.90	1.49	14.85	22.96	1.54	0.19	0.35	3.98
+5%	25.60	46.43	1.81	11.34	20.28	1.79	9.24	15.37	1.66	0.14	0.42	2.96

3.5 Electronic structure

To qualitatively illustrate the variations in the electronic structure of the system with strain, we depicted the calculated E_g as a function of deformation in Fig. 12. When compressive strain is altered from 0% to −5%, a linear rise in E_g from 2.99 to 3.58 eV is found. In contrast, as the tensile strain is adjusted from 0% to +5%, E_g lowers from 2.99 to 2.43 eV. For a quantitative analysis, Fig. 13(a′)/(b′)/(c′) demonstrates the spin-polarized total density of states (TDOS) under varying hydrostatic strain of −5%/0%/+5%. In all three cases, a large E_g between the valence and conduction states is seen, affirming the material's insulating aspect. The progressive reduction of the E_g with augmented tensile strain indicates improved carrier availability around the Fermi level. Along with this, Fig. 13(a)/(b)/(c) illustrates the corresponding electronic band structures for −5%/0%/+5% hydrostatic strain, which closely aligns with the TDOS measurements and further confirms the insulating behavior of the system. All the band structures indicate that E_g is consistently indirect at each strain level because the conduction band minima and valence band maxima are situated at distinct symmetry locations.

3.6 Thermoelectric response

Finally, TE aspects including electrical conductivity per relaxation time $\left(\frac{\sigma}{\tau}\right)$, electronic thermal conductivity per relaxation time $\left(\frac{\kappa_e}{\tau}\right)$, Seebeck coefficient ($S$), power factor $\left(\mathrm{PF} = \frac{\sigma S^2}{\tau}\right)$, lattice thermal conductivity per relaxation time $\left(\frac{\kappa_l}{\tau}\right)$, and figure of merit $\left(ZT = \frac{\sigma S^2 T}{\kappa_e + \kappa_l}\right)$ of the SGH hydride are thoroughly examined for a temperature range of 100–800 K with a consistent τ of 10^{-14} s using the BoltzTraP code[83] and under various hydrostatic strains. Here, it is worth mentioning that we performed an extensive literature survey and found that the relaxation times for similar materials typically fall within 10^{-13} to 10^{-15} s. Therefore, selecting a constant relaxation time of 10^{-14} s represents a reasonable and widely accepted approximation for comparative ZT calculations, allowing us to capture the general thermoelectric trends without introducing undue uncertainty. Thus, a choice of a constant relaxation time of 10^{-14} s can be considered a reasonable and generally accepted approximation to comparative ZT calculations to allow us to describe the overall trends in thermoelectric behavior with a minimum amount of uncertainty. Owing to limitations in the BoltzTraP approach, $\frac{\kappa_e}{\tau}$ can be computed but $\frac{\kappa_l}{\tau}$ cannot. Therefore, we independently determined the $\frac{\kappa_l}{\tau}$ utilizing Slack's equation as follows:[84]

$$\kappa_l = \frac{A M_{av.} \theta_D{}^3 \delta}{\gamma n^{2/3} T} \tag{8}$$

$M_{av.}$, n, T, γ, θ_D, and δ stand for the average atomic mass, number of atoms in the unit cell, absolute temperature, Grüneisen parameter, Debye temperature, and cubic root of the average atomic volume, respectively. Using ν, the Grüneisen parameter (γ) is found as:

$$\gamma = \frac{3(1+\nu)}{2(2-3\nu)} \tag{9}$$

while A is calculated as:[85]

$$A = \frac{2.43 \times 10^{-8}}{1 - \frac{0.514}{\gamma} + \frac{0.228}{\gamma^2}} \tag{10}$$

where θ_D can be established as:[86]

$$\theta_D = \frac{h}{k_B}\left[\frac{3n}{4\pi}\left(\frac{N_A \rho}{M}\right)\right]^{\frac{1}{3}} \times \nu_m \tag{11}$$

wherein h, n, ρ, M, N_A, k_B, and ν_m serve as Plank's constant, the total number of atoms per unit cell, density, molecular weight, Avogadro's number, the Boltzmann constant, and sound velocity, respectively. The average velocity of sound (ν_m) is calculated using:

$$\nu_m = \left[\frac{1}{3}\left(\frac{2}{\nu_l{}^3} + \frac{1}{\nu_t{}^3}\right)\right]^{\frac{-1}{3}} \tag{12}$$

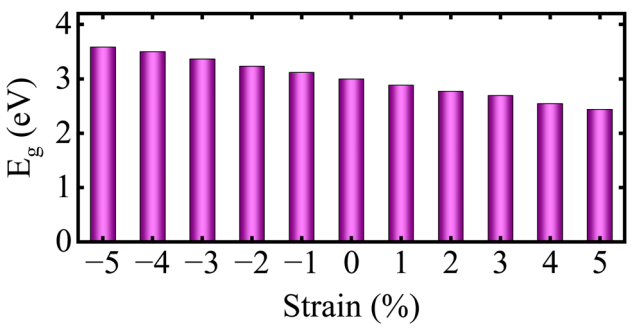

Fig. 12 Computed energy gap (E_g) of the $SrGaH_5$ hydride under ±5% hydrostatic strain.

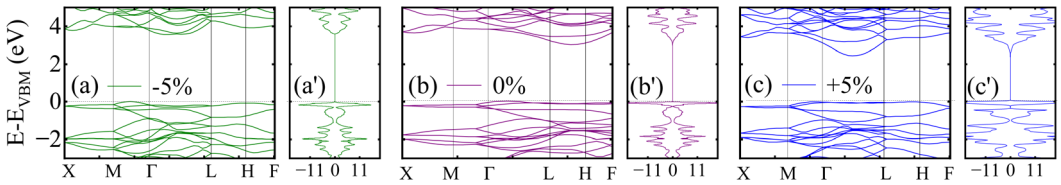

Fig. 13 Computed spin-polarized band structures/total density of states under (a/a′) −5%, (b/b′) 0%, and (c/c′) +5% hydrostatic strains for the $SrGaH_5$ hydride.

The longitudinal/transverse velocity is v_l/v_t, which can be calculated as:

$$v_t = \sqrt{\frac{G}{\rho}} \quad (13)$$

$$v_l = \sqrt{\frac{3B + 4G}{3\rho}} \quad (14)$$

and the corresponding ZT as:

$$ZT = \frac{\sigma S^2 T}{\kappa_e + \kappa_l} \quad (15)$$

The material exhibits significant TE capabilities owing to its considerable E_g and degeneracy in electronic states. Fig. 14(a) illustrates the influence of temperature on $\frac{\sigma}{\tau}$, which increases from 0.21/0.11/0.12 $\times 10^{19}$ 1 Ωm^{-1} s^{-2} at 100 K to 0.37/0.36/0.64 $\times 10^{19}$ 1 Ωm^{-1} s^{-2} at 750 K under −5%/0%/+5% hydrostatic strain. σ is reliant upon the quantity of free carriers. Hence, the rising temperature elevates the quantity of free carriers owing to bond dissociation, thus providing energy to free conduction electrons. Consequently, $\frac{\sigma}{\tau}$ increases with increasing temperature as seen in Fig. 14(a). Among the strain conditions, tensile strain (+5%) provides the greatest $\frac{\sigma}{\tau}$ values, which signifies improved charge carrier mobility or concentration. Conversely, compressive strain (−5%) yields the lowest conductivity, probably owing to enhanced scattering or a decrease in band dispersion. To further assess the efficiency of the material, both κ_e and κ_l were examined at different strain values. The two contributions directly affect the overall thermal conductivity ($\kappa = \kappa_e + \kappa_l$) and consequently the dimensionless ZT. The κ_e (see Fig. 14(b)) exhibits a monotonic rise with elevated temperature throughout, at all strain levels. This tendency is predicted due to the greater mobility of the charge carriers at elevated temperature. It increases from 0.11/0.08/0.09 $\times 10^{14}$ W mK^{-1} s^{-1} at 100 K to 0.39/0.40/1.54 $\times 10^{14}$ W mK^{-1} s^{-1} under −5%/0%/+5% hydrostatic strain. In addition, the computed κ_l decreases with increasing temperature due to enhanced phonon–phonon scattering at elevated thermal energy (see Fig. 14(c)). It decreases from 1.76/2.01/0.9 $\times 10^{14}$ W mK^{-1} s^{-1} at 100 to 0.23/0.26/0.12 W mK^{-1} s^{-1} at 750 K and only reduced further with increasing temperature under −5%/0%/+5% strain. Tensile strain (+5%) results in a significant decrease of κ_l, probably due to enhanced lattice distortion and phonon scattering, which impede thermal conduction across the lattice, which has a positive impact on the ZT value. In contrast, compressive strain (−5%) exhibits marginally elevated values, signifying a partial restoration of lattice order and decreased phonon dispersion.

Fig. 14(d) illustrates the dependence of S on temperature, where its value decreases from 191.03/237.81/219.04 at 100 K to 104.77/97/140 at 750 K. All strained configurations have a positive S, hence confirming p-type conduction. The magnitude of S diminishes with increasing temperature, aligning with the features of degenerate semiconductors. The compressive strain condition has the greatest S, indicating a beneficial alteration in the electronic structure that improves thermopower, likely attributable to a shift in the density of states around the Fermi level. Additionally, Fig. 14(e) displays the PF = $\frac{\sigma S^2}{\tau}$, which combines both σ and S. The value of PF at 100 K is 0.76/0.63/0.57 $\times 10^{11}$ W mK^{-2} s^{-1} and increases to 0.40/0.34/1.27 $\times 10^{11}$ W mK^{-2} s^{-1} under −5%/0%/+5% strain. Likewise, the dimensionless quantity ZT is employed to evaluate the performance of a TE material. Elevated ZT yields enhanced TE reliability, indicating that a greater amount of heat is transformed into electricity. The calculated ZT, as illustrated in Fig. 14(f), demonstrates a progressive increase with temperature from 0.04/0.03/0.05 at 100 K to 0.48/0.37/0.57 at 750 K. However, when the system is subjected to +5% tensile strain, it displays the greatest ZT of 0.61 at 550 K, whereas the unstrained and −5% compressed system demonstrated lower TE efficiency. Hence, these findings highlight the beneficial impact of tensile strain on enhancing TE performance by concurrently augmenting electrical transport and preserving an advantageous S. Finally, it is important to note that a +5% hydrostatic strain is more like a tensile pressure of roughly 3–5 GPa, assuming that there is a normal range of B for such materials. Even though +5% strain is near the upper limit of elasticity of bulk

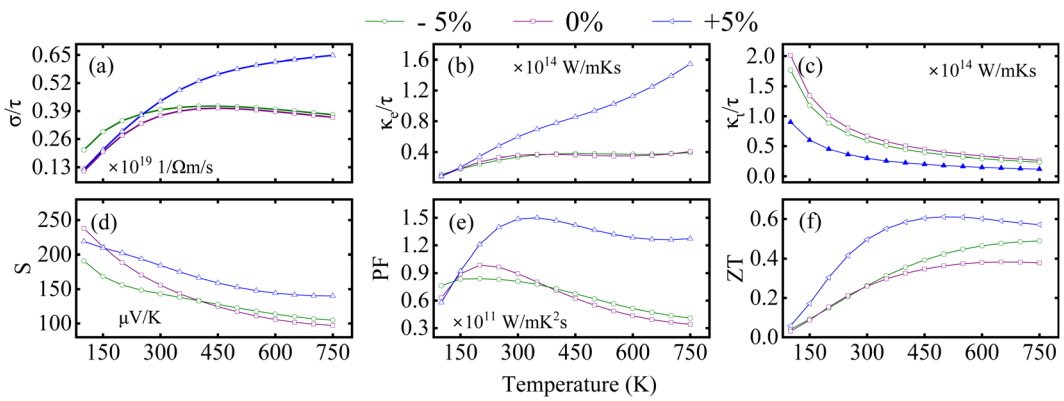

Fig. 14 Various computed thermoelectric parameters under −5%/0%/+5% hydrostatic strain for the $SrGaH_5$ hydride.

systems, +5% strain can be a useful theoretical upper limit to determine sensitivity and tunability of strain. Thus, the estimation of the improvement under the +5% strain gives a good insight into the possible practical strain-engineering approaches.

4 Conclusion

In summary, a first-principles approach utilizing density functional theory was conducted to examine the impact of hydrostatic deformation on the structural, hydrogen storage (HS), mechanical, dynamical, electronic, and thermoelectric (TE) characteristics of the complex $SrGaH_5$ hydride. In comparison to the strain-free system, the deformed motif exhibits enhanced ΔH_f (formation enthalpy) and $T_{des.}$ (desorption temperature) due to strain energy contributions. Specifically, under compressive/tensile tensile strain of −5%/+5%, the ΔH_f reduces from −48.03 kJ per mol H_2 to almost close to an ideal value of −42.93/−45.18 kJ per mol H_2 and the corresponding $T_{des.}$ varies from 343.13 K to 306.67/322.74 K, which lies is in the desired range for HS applications. Additionally, the gravimetric hydrogen storage capacity of the motif is 3.10% and the volumetric hydrogen capacity is 108.89/93.36/80.65 g H_2 per L under −5%/0%/+5% strain, further confirming the system's potential for utilization in HS. Moreover, the electronic structure calculations confirm the insulating behavior of the system, having an indirect band gap of 3.58/2.99/2.43 eV under −5%/0%/+5% hydrostatic strain. Finally, it is found that the TE performance is significantly enhanced under tensile strain with a notable figure of merit of 0.61 achieved at 550 K under +5% strain, indicating superior heat-to-electricity conversion efficiency and improved carrier transport in the studied hydride. Hence, present findings suggest that the examined hydride is not only a promising candidate for HS but also for integration into various energy conversion systems.

Author contributions

Samia Shahzadi: writing – original draft, investigations, formal analysis, data curation A. Ibrahim: visualization, validation, resources, formal analysis. S. Nazir: writing – review and editing, validation, supervision, project administration, conceptualization.

Conflicts of interest

The authors declare no competing interests.

Data availability

The datasets used and/or analyzed during the current study are available from the corresponding author on reasonable request.

Acknowledgements

The authors extend their appreciation to the Deanship of Research and Graduate Studies at King Khalid University for funding this work through Large Research Project under grant number RGP2/713/46.

Notes and references

1 A. S. Oberoi, P. Nijhawan and P. Singh, *Energies*, 2018, **12**, 82.
2 C. H. Tan, P. L. Show, J.-S. Chang, T. C. Ling and J. C.-W. Lan, *Biotechnol. Adv.*, 2015, **33**, 1219–1227.
3 S. Y. Lee, R. Sankaran, K. W. Chew, C. H. Tan, R. Krishnamoorthy, D.-T. Chu and P.-L. Show, *BMC Energy*, 2019, **1**, 1–22.
4 R. Amirante, E. Cassone, E. Distaso and P. Tamburrano, *Energy Convers. Manage.*, 2017, **132**, 372–387.
5 I. P. Jain, *Int. J. Hydrogen Energy*, 2009, **34**, 7368–7378.
6 Z. M. Wang, J. J. Li, S. Tao, J. Q. Deng, H. Zhou and Q. Yao, *J. Alloys Compd.*, 2016, **660**, 402–406.
7 A. Gencer and G. Surucu, *Int. J. Hydrogen Energy*, 2019, **44**, 15173–15182.
8 S. Benlamari, S. Amara Korba, S. Lakel, H. Meradji, S. Ghemid and F. El Haj Hassan, *Int. J. Hydrogen Energy*, 2016, **30**, 1650003.
9 Y. Bouhadda, Y. Boudouma, N. Fennineche and A. Bentabet, *Int. J. Hydrogen Energy*, 2010, **71**, 1264–1268.
10 J. Andersson and S. Grönkvist, *Int. J. Hydrogen Energy*, 2019, **44**, 11901–11919.
11 P. Muthukumar, A. Kumar, M. Afzal, S. Bhogilla, P. Sharma, A. Parida, S. Jana, E. A. Kumar, R. K. Pai and I. Jain, *Int. J. Hydrogen Energy*, 2023, **48**, 33223–33259.
12 I. Jain, C. Lal and A. Jain, *Int. J. Hydrogen Energy*, 2010, **35**, 5133–5144.
13 X. Zhang, Y. Liu, Z. Ren, X. Zhang, J. Hu, Z. Huang, Y. Lu, M. Gao and H. Pan, *Energy Environ. Sci.*, 2021, **14**, 2302–2313.
14 B. Rehmat, M. Rafiq, Y. Javed, Z. Irshad, N. Ahmed and S. Mirza, *Int. J. Hydrogen Energy*, 2017, **42**, 10038–10046.
15 L. Schlapbach and A. Züttel, *Nature*, 2001, **414**, 353–358.
16 M. Al-Zareer, I. Dincer and M. A. Rosen, *Energy Convers. Manage.*, 2018, **157**, 600–618.
17 I. A. Gondal, *Sustainable Energy Fuels*, 2019, **3**, 1468–1489.
18 Y. Bouhadda, Y. Boudouma, N.-E. Fennineche and A. Bentabet, *J. Phys. Chem. Solids*, 2010, **71**, 1264–1268.
19 K. T. Moller, D. Sheppard, D. B. Ravnsbaek, C. E. Buckley, E. Akiba, H.-W. Li and T. R. Jensen, *Energies*, 2017, **10**, 1645.
20 K. Yvon, *Chimia*, 1998, **52**, 613.
21 V. A. Yartys and M. V. Lototskyy, *J. Alloys Compd.*, 2022, **916**, 165219.
22 A. R. Paul, S. Mehla and S. Bhargava, *Small*, 2025, **21**, 2408889.
23 G. Sujan, Z. Pan, H. Li, D. Liang and N. Alam, *Crit. Rev. Solid State Mater. Sci.*, 2020, **45**, 410–427.
24 T. He, H. Cao and P. Chen, *Adv. Mater.*, 2019, **31**, 1902757.
25 Y. Yürüm, A. Taralp and T. N. Veziroglu, *Int. J. Hydrogen Energy*, 2009, **34**, 3784–3798.
26 P. Liu, J. Liang, R. Xue, Q. Du and M. Jiang, *Int. J. Hydrogen Energy*, 2019, **44**, 27853–27861.
27 R. Zacharia and S. U. Rather, *J. Nanomater.*, 2015, **2015**, 914845.

28 A. Schneemann, J. L. White, S. Kang, S. Jeong, L. F. Wan, E. S. Cho, T. W. Heo, D. Prendergast, J. J. Urban, B. C. Wood, *et al.*, *Chem. Rev.*, 2018, **118**, 10775–10839.
29 M. He, Y. Zhang, L. Gong, Y. Zhou, X. Song, W. Zhu, M. Zhang and Z. Zhang, *Int. J. Hydrogen Energy*, 2019, **44**, 28206–28226.
30 A. Siddique, A. Khalil, B. S. Almutairi, M. B. Tahir, T. Ahsan, A. Hannan, H. E. Ali, H. Alrobei and M. Alzaid, *Chem. Phys.*, 2023, **568**, 111851.
31 M. Xiong, C. Lin, Y. Xue and D. Huang, *Inorg. Chem. Commun.*, 2025, **176**, 114264.
32 Y. Song, M. K. Shahzad, S. Hussain, A. Farrukh, M. Riaz, H. Sattar, G. Khan, G. A. Ashraf, S. M. Ali and M. Alam, *Int. J. Hydrogen Energy*, 2024, **79**, 1472–1482.
33 B. Bogdanović and M. Schwickardi, *J. Alloys Compd.*, 1997, **253**, 1–9.
34 G. Meisner, G. Tibbetts, F. Pinkerton, C. Olk and M. Balogh, *J. Alloys Compd.*, 2002, **337**, 254–263.
35 A. Züttel, S. Rentsch, P. Fischer, P. Wenger, P. Sudan, P. Mauron and C. Emmenegger, *J. Alloys Compd.*, 2003, **356**, 515–520.
36 O. Løvvik, S. M. Opalka, H. W. Brinks and B. C. Hauback, *Phys. Rev. B:Condens. Matter Mater. Phys.*, 2004, **69**, 134117.
37 P. Chen and M. Zhu, *Mater. Today*, 2008, **11**, 36–43.
38 B. B. Kitchen, N. Verdal, T. J. Udovic, J. J. Rush, M. R. Hartman and D. J. DeVries, *J. Solid State Chem.*, 2013, **203**, 51–54.
39 P. Vajeeston, P. Ravindran, A. Kjekshus and H. Fjellvåg, *J. Alloys Compd.*, 2005, **387**, 97–104.
40 V. Balema, J. Wiench, K. Dennis, M. Pruski and V. Pecharsky, *J. Alloys Compd.*, 2001, **329**, 108–114.
41 A. Finholt, A. Bond Jr and H. Schlesinger, *J. Am. Chem. Soc.*, 1947, **69**, 1199–1203.
42 S. Orimo, Y. Nakamori and A. Züttel, *Mater. Sci. Eng., B*, 2004, **108**, 51–53.
43 N. S. Norberg, T. S. Arthur, S. J. Fredrick and A. L. Prieto, *J. Am. Chem. Soc.*, 2011, **133**, 10679–10681.
44 F. Zhang, Y. Wang and M. Chou, *J. Am. Chem. Soc.*, 2012, **116**, 18663–18668.
45 C. Mui, S. F. Bent and C. B. Musgrave, *J. Phys. Chem. B*, 2004, **108**, 6336–6350.
46 H. Benzidi, M. Lakhal, M. Abdellaoui, M. Garara, A. Benyoussef, M. Loulidi, M. Hamedoun, O. Mounkachi, *et al.*, *Int. J. Hydrogen Energy*, 2019, **44**, 16793–16802.
47 E. German and R. Gebauer, *J. Phys. Chem. C*, 2016, **120**, 4806–4812.
48 B. W. Chen and M. Mavrikakis, *Nano Energy*, 2019, **63**, 103858.
49 F. S. Sangsefidi and M. Salavati-Niasari, *ACS Appl. Energy Mater.*, 2018, **1**, 4840–4848.
50 H. Benzidi, M. Lakhal, A. Benyoussef, M. Hamedoun, M. Loulidi, O. Mounkachi, *et al.*, *Int. J. Hydrogen Energy*, 2017, **42**, 19481–19486.
51 J.-J. Tang, X.-B. Yang, M. Chen, M. Zhu and Y.-J. Zhao, *J. Phys. Chem. C*, 2012, **116**, 14943–14949.
52 J. Zhang, Y. Zhou, Z. Ma, L. Sun and P. Peng, *Int. J. Hydrogen Energy*, 2013, **38**, 3661–3669.
53 M. Garara, H. Benzidi, M. Abdellaoui, M. Lakhal, A. Benyoussef, O. Mounkachi, M. Loulidi, *et al.*, *Mater. Chem. Phys.*, 2020, **254**, 123417.
54 M. Rkhis, S. Laasri, S. Touhtouh, E. Hlil, M. Bououdina, R. Ahuja, K. Zaidat, S. Obbade and A. Hajjaji, *Int. J. Hydrogen Energy*, 2022, **47**, 3022–3032.
55 C. Weidenthaler, T. J. Frankcombe and M. Felderhoff, *Inorg. Chem.*, 2006, **45**, 3849–3851.
56 A. Klaveness, P. Vajeeston, P. Ravindran, H. Fjellvåg and A. Kjekshus, *Phys. Rev. B:Condens. Matter Mater. Phys.*, 2006, **73**, 094122.
57 A. Klaveness, O. Swang, A. Kjekshus and H. Fjellvåg, *Inorg. Chem.*, 2006, **45**, 10698–10701.
58 P. Blaha, K. Schwarz, P. Sorantin and S. Trickey, *Comput. Phys. Commun.*, 1990, **59**, 399–415.
59 J. P. Perdew, K. Burke and M. Ernzerhof, *Phys. Rev. Lett.*, 1996, **77**, 3865.
60 F. D. Murnaghan, *Proc. Natl. Acad. Sci. U. S. A.*, 1944, **30**, 244–247.
61 C. Yang, Y. Duan, X. Wang, M. Peng, L. Shen and H. Qi, *Mater. Today Commun.*, 2022, **32**, 103962.
62 A. Arharbi, H. Jebari and H. Ez-Zahraouy, *J. Energy Storage*, 2025, **106**, 114903.
63 A. Arharbi and H. Ez-Zahraouy, *Int. J. Hydrogen Energy*, 2024, **65**, 262–270.
64 H. Ez-Zahraouy, *et al.*, *Int. J. Hydrogen Energy*, 2024, **87**, 678–685.
65 M. Ramzan, S. Lebegue and R. Ahuja, *Int. J. Hydrogen Energy*, 2010, **35**, 10373–10376.
66 R. Gremaud, C. P. Broedersz, D. M. Borsa, A. Borgschulte, P. Mauron, H. Schreuders, J. H. Rector, B. Dam and R. Griessen, *Adv. Mater.*, 2007, **19**, 2813–2817.
67 Y. Liu, Y. Jiang, R. Zhou and J. Feng, *J. Alloys Compd.*, 2014, **582**, 500–504.
68 V. Kudiiarov, J. Lyu, O. Semyonov, A. Lider, S. Chaemchuen and F. Verpoort, *Appl. Mater. Today*, 2021, **25**, 101208.
69 C. Zhou, R. C. Bowman Jr, Z. Z. Fang, J. Lu, L. Xu, P. Sun, H. Liu, H. Wu and Y. Liu, *ACS Appl. Mater. Interfaces*, 2019, **11**, 38868–38879.
70 J. Willems, *Z. Phys. Chem.*, 1986, **147**, 231.
71 N. Xu, Y. Chen, S. Chen, S. Li and W. Zhang, *Int. J. Hydrogen Energy*, 2024, **50**, 114–122.
72 M. Baaddi, R. Chami, O. Baalla, S. E. Quaoubi, A. Saadi, L. E. H. Omari and M. Chafi, *Environ. Sci. Pollut. Res.*, 2024, **31**, 62056–62064.
73 I. Rhrissi, A. Bouhmouche and R. Moubah, *Int. J. Hydrogen Energy*, 2025, **117**, 146–157.
74 X. Wu, D. Vanderbilt and D. Hamann, *Phys. Rev. B:Condens. Matter Mater. Phys.*, 2005, **72**, 035105.
75 S. Shang, Y. Wang and Z.-K. Liu, *Appl. Phys. Lett.*, 2007, **90**, 101909.
76 F. Mouhat and F.-X. Coudert, *Phys. Rev. B:Condens. Matter Mater. Phys.*, 2014, **90**, 224104.
77 S. Pugh, *Lond. Edinb. Dubl. Phil. Mag.*, 1954, **45**, 823–843.
78 G. Surucu, *Mater. Chem. Phys.*, 2018, **203**, 106–117.
79 A. Gencer and G. Surucu, *Mater. Res. Express*, 2018, **5**, 076303.

80 S. Yalameha, Z. Nourbakhsh and D. Vashaee, *Comput. Phys. Commun.*, 2022, **271**, 108195.
81 C. Ekuma and Z.-L. Liu, *Comput. Phys. Commun.*, 2024, **300**, 109161.
82 Y. Lv, X. Zhang and W. Jiang, *Ceram. Int.*, 2018, **44**, 128–135.
83 G. K. H. Madsen and D. J. Singh, *Comput. Phys. Commun.*, 2006, **175**, 67–71.
84 J. Wei, Y. Guo and G. Wang, *RSC Adv.*, 2023, **13**, 11513–11524.
85 S. A. Sofi and D. C. Gupta, *Int. J. Energy Res.*, 2021, **45**, 4652–4668.
86 O. L. Anderson, *J. Phys. Chem. Solids*, 1963, **24**, 909–917.